

## Statistical maps of small-scale electric field variability in the high-latitude ionosphere

E. D. P. Cousins<sup>1</sup> and S. G. Shepherd<sup>1</sup>

Received 9 May 2012; revised 26 September 2012; accepted 19 October 2012; published 8 December 2012.

[1] Statistical maps of small-scale electric field variability in the high-latitude ionosphere are derived for the Northern and Southern Hemispheres using 48 months of data from the Super Dual Auroral Radar Network (SuperDARN). Maps of variability magnitude (from scales of 45–450 km and 2–20 min) are derived for a range of interplanetary magnetic field (IMF) orientations and dipole tilt angles (the angle between the best fit dipole axis and the plane perpendicular to the Sun–Earth line). It is found that the observed spatial distribution of average variability is significantly modified as the IMF and dipole tilt conditions change. Under negative (winter-like) and neutral (equinox-like) dipole tilt angles, variability is concentrated in the auroral and dayside cusp regions, and the spatial distributions of variability appear to be correlated to those of large- and small-scale field-aligned currents (FACs). Additionally, variability on the nightside is found to be more enhanced in the downward FAC region than it is in the upward FAC region. Under positive (summer-like) dipole tilt angles, the average variability magnitudes across the high-latitude regions are smaller than those observed under negative dipole tilt angles, and the spatial distributions are more uniform. These dipole tilt effects suggest that scale-size- and conductivity-dependent field-aligned potential drops and conductivity-dependent changes in the processes that generate variability are possible factors that impact the observed small-scale electric field variability. In general, Southern Hemisphere maps appear very similar to Northern Hemisphere maps, although some minor differences are observed that may result from interhemispheric asymmetries in the geomagnetic field.

**Citation:** Cousins, E. D. P., and S. G. Shepherd (2012), Statistical maps of small-scale electric field variability in the high-latitude ionosphere, *J. Geophys. Res.*, 117, A12304, doi:10.1029/2012JA017929.

### 1. Introduction

[2] Electric fields in the high-latitude regions of the Earth's ionosphere are one important component of the coupled magnetosphere-ionosphere-thermosphere system. These electric fields are largely driven by magnetospheric electric fields and currents, which are in turn driven by interactions between the magnetosphere and the solar wind. The ionospheric electric fields, which are associated with plasma drifts, inject energy into the thermosphere through collisions between the drifting plasma and the neutral atmosphere.

[3] Through characterizing the dependence of high-latitude electric fields on solar wind or geomagnetic conditions, many statistical or empirical models of these fields have been derived [e.g., Papitashvili *et al.*, 1999; Ruohoniemi and Greenwald, 2005; Weimer, 2005; Zhang *et al.*, 2007; Cousins and Shepherd, 2010]. These models are used in

addition to or in place of instantaneous measurements when knowledge of the complete configuration of high-latitude electric fields is required. They are also used as inputs to numerical models of neighboring regions, such as the thermosphere [e.g., Fuller-Rowell and Rees, 1980; Roble *et al.*, 1988; Ridley *et al.*, 2006].

[4] The empirical models typically used as inputs to thermosphere global circulation models (GCMs), however, only reproduce the large-scale, smooth, high-latitude convection pattern and they do not reproduce the variability seen in electric field observations [e.g., Matsuo *et al.*, 2002, 2003; Codrescu *et al.*, 2000]. The exclusion of such variability has been cited as a possible source of discrepancies between modeled and observed thermospheric behavior [e.g., Codrescu *et al.*, 1995; Fesen *et al.*, 1999; Deng and Ridley, 2007; Codrescu *et al.*, 2008; Fedrizzi *et al.*, 2012]. The impact of electric field variability has been investigated using thermosphere GCMs and it is found that the energy and momentum that is input to the atmosphere can increase by as much as 100% when variability is included in the specified high-latitude electric fields [e.g., Codrescu *et al.*, 2000; Matsuo and Richmond, 2008; Deng *et al.*, 2009].

[5] The variability in high-latitude electric fields is often considered to have two components: variations on scale sizes below the resolution of statistical or empirical models (small-scale variability) and variations on scales sizes at

<sup>1</sup>Thayer School of Engineering, Dartmouth College, Hanover, New Hampshire, USA.

Corresponding author: E. D. P. Cousins, Thayer School of Engineering, Dartmouth College, Hanover, NH 03755, USA. (ellen.cousins@dartmouth.edu)

©2012. American Geophysical Union. All Rights Reserved. 0148-0227/12/2012JA017929

or above the model resolution (resolved-scale variability) [Cosgrove *et al.*, 2011]. The characteristics of resolved-scale variability depend on the background statistical or empirical model being used, while small-scale variability is a physical quantity that depends on the selected statistical model only for the definition of the upper scale-size limit, which is typically on the order of 100 km and 10 min. Such small-scale electric field variability is the focus of this study, where small scale is defined to be between 45 and 450 km and between 2 and 20 min.

[6] The statistical properties of small-scale electric field or velocity variability have been investigated using data from the Dynamics Explorer (DE) 2 low-altitude satellite [Heppner *et al.*, 1993; Golovchanskaya *et al.*, 2002; Johnson and Heelis, 2005; Golovchanskaya *et al.*, 2006; Golovchanskaya, 2007; Matsuo and Richmond, 2008] and from ground-based coherent backscatter radars [Abel *et al.*, 2007, 2009; Parkinson, 2008; Cousins and Shepherd, 2012]. In these studies, the observed variability is found to depend on scale size, on season or dipole tilt angle, on gradients or shears in the background plasma drift and on location in geomagnetic coordinates. Several studies have also derived maps of the magnitude of small-scale electric field variability in the high-latitude region [Golovchanskaya *et al.*, 2006; Golovchanskaya, 2007; Matsuo and Richmond, 2008], finding that the spatial distribution of variability magnitudes changes with season and with the orientation of the interplanetary magnetic field (IMF). Note that these variability maps were all derived using satellite data (from DE 2), which cannot distinguish between spatial and temporal variations in the observed electric fields.

[7] This study expands the work of Cousins and Shepherd [2012] and, using data from the Super Dual Auroral Radar Network (SuperDARN), derives statistical maps of small-scale electric field variability that show important properties of the spatial distribution of this variability. Section 2 describes the method used to create small-scale variability maps, section 3 describes the important properties of the maps, and section 4 discusses possible origins of the observed variability properties.

## 2. Technique

[8] The techniques used to calculate small-scale electric field variability and to derive statistical maps of variability are described in this section. These techniques are similar to those used by Golovchanskaya *et al.* [2006], Golovchanskaya [2007], and Matsuo and Richmond [2008] with DE-2 data in that small-scale variability data is calculated, sorted by seasonal and solar wind conditions, and averaged onto a grid in geomagnetic coordinates. The method of calculating variability, however, is different in this study (velocity differences are measured over small spatial scales as opposed to the high-pass filtering of time series) and the amount of data available is much larger (6 years of data from 10 to 16 radars as opposed to 1.5 years of data from a single satellite), capturing many seasons over almost half a solar cycle and enabling, for example, independent treatment of the two hemispheres.

### 2.1. Calculating Variability

[9] The small-scale electric field variability data used in this study are derived using the technique described by

Cousins and Shepherd [2012], which is summarized briefly here. The basis of this study is data provided by the SuperDARN high-frequency, coherent backscatter radars, which are located in the high-latitude regions of the Northern and Southern Hemispheres. Each radar included in this study has a  $\sim 50^\circ$  field of view (FOV) and transmits along 16 electronically steered beams within that region, with 75 range gates used along each beam. These radars measure the line-of-sight (LOS) component of the  $\mathbf{E} \times \mathbf{B}$  drift of plasma in the  $F$  region ionosphere. All the velocity data used in this study have a spatial resolution of 45 km in the LOS direction, with a time cadence of 2 min. For each beam at each time step, up to 75 velocity measurements are recorded, corresponding to a spatial coverage of up to 3375 km in the LOS direction.

[10] For this study, 48 months of data (8 months per year) are used from 1999 to 2004 (around the maximum of solar cycle 23). In the Northern Hemisphere, data from February, April, May, June, July, August, October, and December are included from each year, while in the Southern Hemisphere, January, February, April, June, August, October, November, and December are included. Because of the tremendous amount of data available from all the SuperDARN radars, adequate counting statistics can be achieved without the use of all 12 months of data per year. The use of one winter month, two fall and two spring months, and three summer months results in a roughly equal distribution of data across the seasons because generally less backscatter is observed during summer months and more backscatter is observed during winter months [e.g., Ruohoniemi and Greenwald, 1997]. As discussed in section 3, the particular selection of months has an insignificant impact on the derived variability maps.

[11] During the years considered in this study, 6–9 radars in the Northern Hemisphere and 4–7 radars in the Southern Hemisphere were operational. The data coverage from these radars spans all local times and  $\sim 65^\circ$ – $90^\circ$  geomagnetic latitude in both hemispheres.

[12] Several criteria are imposed on the data to ensure that only consistent and high-quality measurements from the  $F$  region ionosphere are included in the variability calculation. In order to ensure that all velocity measurements have the same spatial and temporal resolution, only data from the normal 2 min operating mode of the radars are included. Furthermore, data are excluded if the signal-to-noise ratio of the backscatter is less than 3 dB, if the velocity error is greater than 150 m/s, or if the data are statistically likely to be  $E$  region scatter or ground scatter. A complete description of this conditioning is given by Cousins and Shepherd [2012].

[13] Two types of variability are considered independently: small-scale spatial variability and small-scale temporal variability. The spatial and temporal variability at a given point is quantified by calculating velocity fluctuations (differences in velocity) between the given point and its neighbors, separated by up to  $\pm 450$  km and up to  $\pm 20$  min. The velocity fluctuations are defined as  $\Delta v_r(\Delta r) = v_{los}(r + \Delta r, t) - v_{los}(r, t)$  and  $\Delta v_t(\Delta t) = v_{los}(r, t + \Delta t) - v_{los}(r, t)$ , with  $\Delta r$  ranging from  $\pm 45$  km to  $\pm 450$  km and  $\Delta t$  ranging from  $\pm 2$  min to  $\pm 20$  min. Using this definition, up to 20 fluctuation samples ( $\pm 10$  increments of 2 min or 45 km) are available in each domain (space and time) at a given point ( $r, t$ ). To avoid the

inclusion of erroneous outliers in this study, fluctuations greater than  $\sim 3\sigma$  (1200 m/s), where  $\sigma$  is the standard deviation of the unconditioned fluctuations, are excluded. Additionally, points with fewer than 7 out of the 20 possible neighboring velocity measurements are likely to be noise and are also excluded.

[14] The amount of data available in the study is sufficiently large as to require that some form of data reduction technique be applied. To achieve unbiased data reduction, one  $\Delta v_r$  and one  $\Delta v_t$  value is randomly selected out of the up to 20 values in each domain (space and time), following the standard statistical technique of stratified random sampling. Random selection is used instead of an average or median in order to preserve the original distribution shape of the fluctuation data, which is significantly modified when medians or averages are used to reduce the data.

[15] Finally, these values are converted from velocity to electric field using the relation  $\mathbf{V} = \mathbf{E} \times \mathbf{B}/B^2$ , where  $\mathbf{B}$  is given by the International Geomagnetic Reference Field (IGRF-11). This procedure for calculating variability is explained and illustrated in more detail by *Cousins and Shepherd* [2012].

[16] It should be noted that, due to the rotation of the Earth, the ground-based radars travel in local time and MLT during an increment of time,  $\Delta t$ . As a result, the temporal electric field fluctuations observed by the radars could include space as well as time variations. As described by *Cousins and Shepherd* [2012], however, it is found that the temporal fluctuations observed by the radars are in fact dominated by time variations for a majority of the observations.

## 2.2. Deriving Variability Maps

[17] Using the database of electric field variability measurements described in section 2.1, *Cousins and Shepherd* [2012] investigated the statistical characteristics of small-scale variability. It was found that the variability displays turbulent behavior and that the magnitudes of variability are significantly correlated to gradients or shears in the background velocity, to season and solar cycle, and to location in geomagnetic coordinates. In this study, we focus on the spatial distribution of variability across the high-latitude regions of the two hemispheres. Maps of average variability magnitudes in both hemispheres are derived for a variety of solar wind and season-like (dipole tilt angle) conditions. The parameters used to sort the data are selected based on the dependencies described by *Cousins and Shepherd* [2012]. Although *Cousins and Shepherd* [2012] observed that the seasonal dependence of variability appears stronger near solar maximum and weaker near solar minimum, this solar cycle dependence is ignored when deriving variability maps. This dependence is omitted because the variability data set spans approximately half a solar cycle and separating the true solar cycle dependence from other possible affects is not feasible without observations from more than one cycle.

[18] To define the variability maps, the fluctuation data are first sorted into three “seasonal” categories based on dipole tilt angle and then further sorted into four IMF categories based on the upstream IMF clock angle. Spatial and temporal fluctuation data are treated independently and Northern Hemisphere and Southern Hemisphere data are also treated independently.

[19] The dipole tilt angle is defined as the magnitude of the angle between the Earth’s best fit magnetic dipole axis and the geocentric solar magnetospheric (GSM) y-z plane from IGRF and is hereafter referred to simply as tilt. The sign is set such that positive and negative tilt corresponds to sunlit and dark conditions, respectively. The IMF clock angle is defined as  $\tan^{-1}(B_y/B_z)$ , where  $B_y$  and  $B_z$  are the y and z components of the IMF in GSM coordinates, respectively. Solar wind data are obtained from the 1 min resolution OMNI database [*King and Papitashvili*, 2005] and, as explained by *Cousins and Shepherd* [2012], the values of the interplanetary parameters are averaged over the 60 min prior to the time of measurement.

[20] The three seasonal categories are defined as tilt  $< -10^\circ$ ,  $|\text{tilt}| \leq 10^\circ$ , and tilt  $> 10^\circ$ , corresponding to winter-like (“winter”), equinox-like (“equinox”), and summer-like (“summer”) conditions. Due to the offset between the Earth’s dipole and spin axes, however, there is not a one-to-one correspondence between tilt and true season, and *Cousins and Shepherd* [2012] found that small-scale variability is more strongly correlated to tilt than it is to season. Note that the tilt angle categories used here are the same as those used by *Pettigrew et al.* [2010] to derive maps of large-scale convection. The four IMF clock angle categories are centered about  $0^\circ$  ( $B_z+$ ),  $90^\circ$  ( $B_y+$ ),  $180^\circ$  ( $B_z-$ ), and  $270^\circ$  ( $B_y-$ ) and are  $90^\circ$  wide. No sorting by the solar wind velocity, the transverse magnitude of the IMF or the geomagnetic activity indices  $Kp$  or AE is performed because these parameters are found to have no significant correlation with average variability magnitudes [*Cousins and Shepherd*, 2012].

[21] For each of the 12 possible categories per hemisphere, per domain (spatial or temporal), the variability data are arranged onto an equal-area spatial grid with a  $1^\circ$  resolution in geomagnetic latitude. Altitude adjusted corrected geomagnetic (AACGM) coordinates [*Baker and Wing*, 1989] are used to define the grid. Figure 1a shows the number of data points contained in each grid cell for one category (negative tilt, IMF  $B_y+$  conditions) in the Northern Hemisphere. The data counts shown in Figure 1a, which range from  $\sim 1,000$  to  $> 100,000$ , are representative of those seen in other IMF  $B_y$  categories. The counts for the IMF  $B_z$  categories are slightly lower than those for the IMF  $B_y$  categories due to fewer time periods with dominant IMF  $B_z$  conditions. In general, the data counts peak on the nightside in MLT and near  $70^\circ$  geomagnetic latitude, falling off toward the pole and toward lower latitudes. On the dayside, counts tend to be confined to higher latitudes.

[22] For each of the grid cells containing sufficient data (3000 points in the Southern Hemisphere or 5000 points in the Northern Hemisphere, which has more radars), the normalized probability density function (pdf) of the fluctuation data in that cell is calculated and fit to an exponential distribution given by  $p(x) = (1/\mu) * e^{-x/\mu}$ , where  $x$  is the electric field fluctuation in mV/m and  $\mu$  is the mean of the exponential distribution in mV/m. This distribution is selected to represent the data based on the results of *Cousins and Shepherd* [2012], who found that observed electric field fluctuations could be well represented by an exponential distribution. Fitting the pdf to this functional form, rather than simply defining the mean of the exponential distribution ( $\mu$ ) to be the arithmetic mean of the fluctuations,

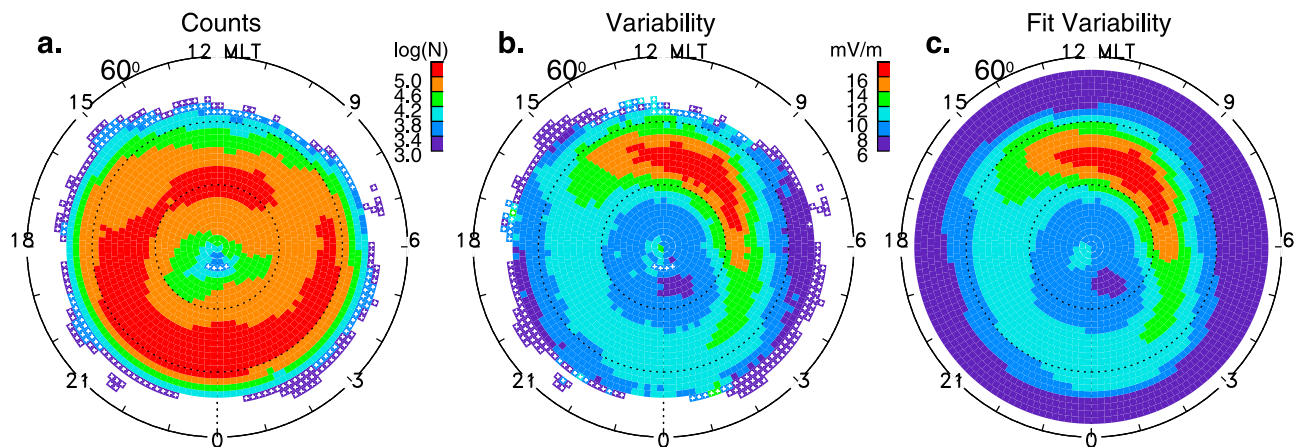


**Figure 1.** Maps of (a) the number of data points (on a logarithmic scale), (b) the mean variability value, and (c) the fit variability value in  $\sim 110 \times 110$  km grid cells for negative tilt, IMF  $B_y+$  conditions in the Northern Hemisphere. The maps are plotted in geomagnetic coordinates.

is performed because the observed distribution is not exactly exponential [Cousins and Shepherd, 2012] and, as discussed in section 2.1, the distribution is truncated at 60 mV/m (1200 m/s). As a result, using the arithmetic mean to define a representative exponential distribution would result in a consistent underestimation of the root-mean-square (RMS) average of the fluctuation magnitudes by  $\sim 15\%$ .

[23] Figure 2 shows an example of a typical pdf with an exponential fit shown by the dotted red line. The RMS average of the best fit exponential distribution (indicated by the vertical dashed red line in Figure 2) closely approximates the RMS average of the observed fluctuations (indicated by the vertical dashed black line). The RMS average of an exponential distribution that is defined by the arithmetic mean of the observed fluctuations is smaller than these values, as indicated by the vertical dashed blue line.

[24] Applying this procedure to each grid cell results in maps of the variability magnitude across the high-latitude region. An example variability map for the data shown in Figure 1a is given in Figure 1b, in which color indicates the value of  $\mu$  in each grid cell. Small white crosses indicate cells where  $\mu$  is defined by the arithmetic mean because there is insufficient data to calculate and fit a functional form to the pdf. For reference, these white crosses are also shown on the map of data counts given in Figure 1a. These low-data cells are typically located at low latitudes (near the radar locations) and near the pole (at far ranges from the radars).

[25] Comparing maps of average variability with maps of data counts, such as Figures 1b and 1a, shows that the spatial distribution of the observed variability is generally uncorrelated to that of the data counts. Regions of large average variability are not associated with either high or low data counts, and regions with large data counts are not associated with either high or low variability. One exception to this lack of correlation is in regions with very little data ( $< \sim 1000$  points), such as at the lowest latitudes and in the high polar cap for IMF  $B_z$  categories, where lower data counts can be correlated with larger variability.

[26] Average variability maps like that shown in Figure 1b are useful for illustrating the spatial distribution of observed variability. However, in order to conveniently and efficiently represent these maps in a form that behaves continuously

across the entire high-latitude region, each variability map is fit to an expansion of spherical harmonics. Spherical harmonic fitting is a standard technique for deriving representative maps of ionospheric data [e.g., Ruohoniemi and Greenwald, 1998] and the details of the fitting are briefly described here. The order and degree of the spherical harmonic expansion is set to 10, which is empirically determined to be the lowest order that can best reproduce the observed variability patterns. This expansion has a resolution of  $\sim 2.5^\circ$  geomagnetic latitude and 2.4 h magnetic local time (MLT). Using a lower-order expansion results in larger errors in the fit while using a higher-order expansion tends to result in ringing in regions not well constrained by data, such as in the high polar cap. As discussed later in this section, the selected resolution is sufficient to well reproduce the

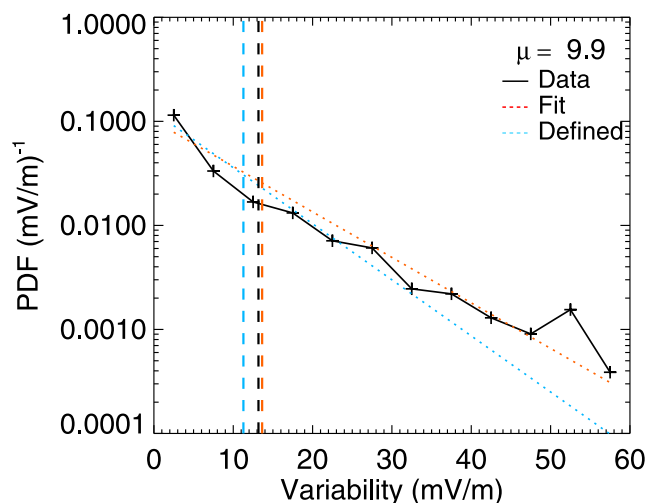


**Figure 2.** Normalized pdf of fluctuation data in an example cell from Figure 1a, showing a typical exponential fit. The dotted lines show the (red) best fit exponential distribution and the (blue) exponential distribution defined by the arithmetic mean. Vertical dashed lines indicate the RMS averages of the (black) observed, (red) fit, and (blue) defined distributions. The mean of the best fit exponential is given at top right.

features observed in the average variability maps. The lower-latitude limit of the expansion is automatically determined based on the distribution of the data and is typically  $\sim 65^\circ$ . In the fitting procedure, the variability values are error weighted according to their statistical uncertainty, determined by bootstrap error estimation [e.g., *Efron and Tibshirani*, 1993].

[27] Several constraints are imposed to ensure that the best fit solution is well behaved across the entire high-latitude region. Near the equatorward and poleward limits of the observations, average variability values that are very large compared to typical values are occasionally observed. These large averages are likely due to the lower data counts in these regions, which allow the average to be strongly impacted by large values due to noise or unusual events. If these large average values are classified as outliers compared to their neighbors, they are excluded from the fitting procedure. Additionally, in the positive tilt maps the distribution of data is confined to significantly higher latitudes on the dayside than on the nightside. To prevent the fit solution from becoming unphysically large in this unconstrained region, zero padding is added on the dayside for the positive tilt categories, following the method of *Shepherd and Ruohoniemi* [2000]. Finally, data coverage tends to decrease significantly near the poles ( $> \sim 85^\circ$ ). If gaps occur in the data coverage in this region, values are estimated by interpolating between neighboring grid cells in order to prevent the fitted solution from becoming unphysical. All of these constraints serve to keep the fitted solution from becoming unphysical in regions not well constrained by data without impacting other, well-constrained regions.

[28] Figure 1c shows the best fit solution for the average variability map given in Figure 1b, corresponding to negative tilt, IMF  $B_y+$  conditions in the Northern Hemisphere. This fitted variability map appears somewhat smoother than the original data because the order of the spherical harmonic expansion is such that the resolution of the fitted map is lower than that of the original map. Aside from this smoothing effect, the features of the fitted map are in excellent agreement with all the features seen in Figure 1b, and a similar agreement is seen between fitted and original variability maps for the other IMF and tilt categories. For all categories, the RMS error between the fitted and original variability maps is  $\leq 1$  mV/m. This agreement suggests that, at least in an average sense, small-scale variability and the factors that control it tend to be organized on a scale of several hundreds of kilometers or larger (the resolution of the fitted expansion).

### 3. Results

[29] Using the procedure described in section 2.2, fitted maps of small-scale variability are derived for all 12 dipole tilt and IMF clock angle categories in both hemispheres. Variability maps are derived for spatial and temporal electric field variability independently and it is found that maps of temporal variability have the same large-scale spatial features and similar average magnitudes as those of spatial variability. A detailed comparison of spatial and temporal variability was performed by *Cousins and Shepherd* [2012], who noted some differences between the two but observed that the general behaviors and average magnitudes of spatial

and temporal variability are very similar. These similarities are consistent with the theory that, at least at larger scale sizes, temporal variability results in large part from connecting static structures [e.g., *Ishii et al.*, 1992; *Earle and Kelley*, 1993; *Knudsen et al.*, 1990]. Because of these similarities, we focus only on spatial variability maps here, noting that the results described below generally apply to temporal variability as well.

[30] Figure 3 shows the spatial variability maps for all IMF clock angle categories for negative, neutral, and positive tilt conditions, with color indicating the fitted average variability magnitude. The maps are derived independently in the Northern and Southern Hemispheres. The average variability magnitude across the region is given at the bottom left of each map.

[31] It should be noted that, as described in section 2.1, these maps are derived using only 8 months of data per year. In particular, only two months are used for each equinox season and the months of March and September are excluded. To investigate the impact that the selection of these particular months has on the derived variability maps, the “equinox” maps for the Northern Hemisphere were also derived independently using data from March and September and excluding February and August instead. Comparing the maps derived using the different selection of months, it is found that for all IMF clock angle categories the magnitude of the average difference between the maps is less than 0.2 mV/m and the RMS difference is smaller than the error associated with the fitting procedure and is thus considered to be insignificant. The differences between these maps are largest in regions not well constrained by data (i.e.,  $> 85^\circ$  and  $< 68^\circ$  latitude) and are small ( $\leq 0.5$  mV/m) in well-constrained regions.

[32] From the maps shown in Figure 3, it is clear that the magnitude of small-scale electric field variability depends on geomagnetic latitude, MLT, IMF clock angle, and dipole tilt. Variability magnitudes are generally largest in auroral zone latitudes ( $\sim 70^\circ$ – $80^\circ$ ) and in the dayside and dawnside in MLT. Considering the IMF clock angle dependence, for IMF  $B_z-$  conditions, variability tends to decrease quickly above  $\sim 80^\circ$  latitude while for IMF  $B_z+$  conditions, moderate variability can still be observed across the entire polar cap. Additionally, as the direction of IMF  $B_y$  changes from  $B_y+$  ( $B_y-$ ) to  $B_y-$  ( $B_y+$ ) in the north (south), the location of peak variability rotates in MLT from prenoon to postnoon. While the spatial distribution of variability magnitudes depends on IMF clock angle, the overall average variability magnitude (given at the bottom left of each map in Figure 3) shows no significant or consistent dependence on IMF clock angle. This lack of dependence is consistent with the observation that average variability magnitudes are not correlated with geomagnetic activity indices such as  $K_p$  or AE [*Cousins and Shepherd*, 2012].

[33] Considering the tilt dependence, for all IMF conditions shown in Figure 3, magnitudes of variability are on average smaller for positive tilt (“summer”) than for negative tilt (“winter”). Maps of electric field variability for neutral tilt more closely resemble negative tilt maps than positive tilt maps. The average magnitudes of variability for neutral tilt are approximately the same as or slightly larger than (by up to 9%) negative tilt magnitudes. Note that the errors in the SuperDARN measurements are much smaller

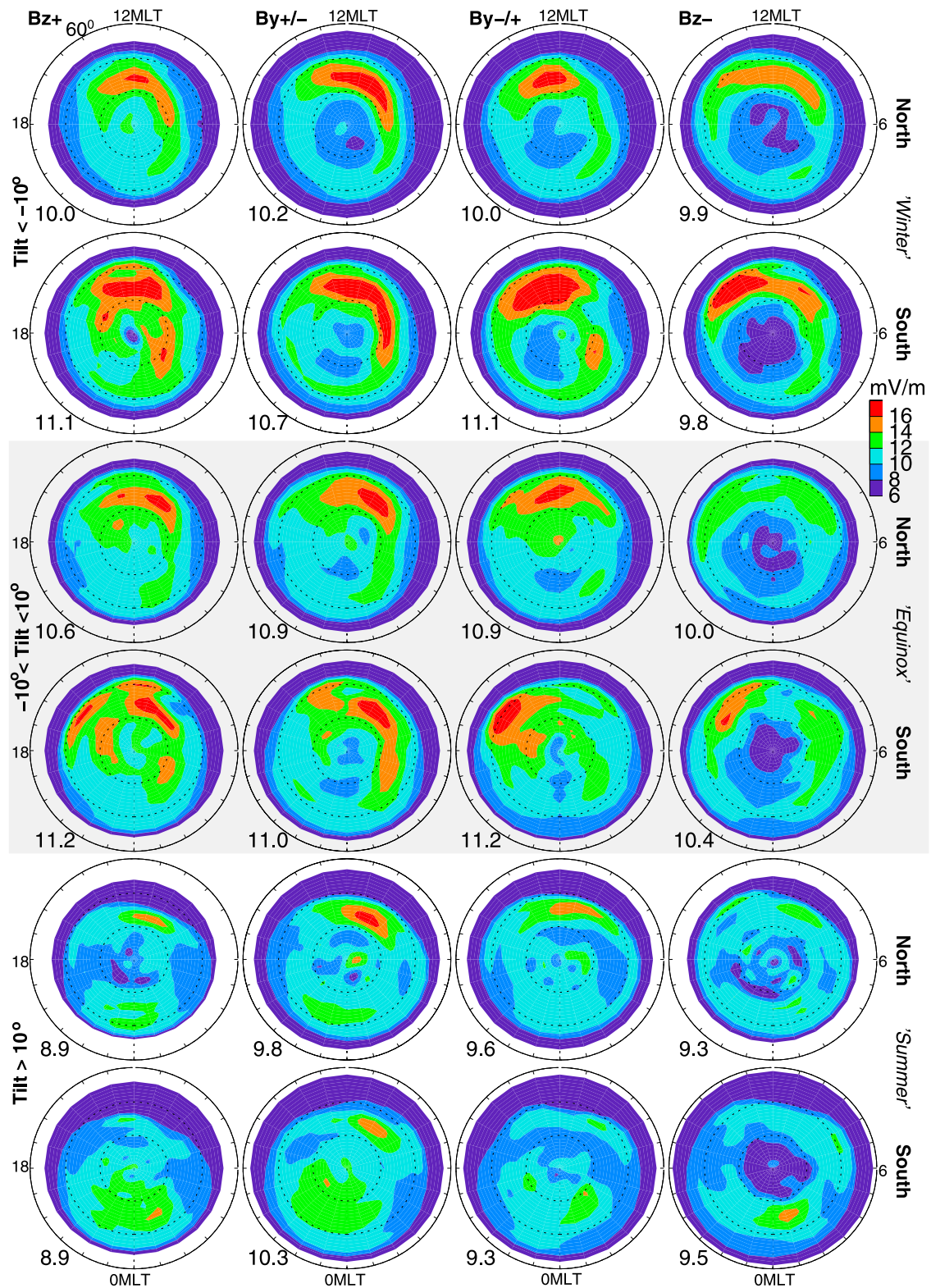


**Figure 3.** Fitted average magnitudes of small-scale spatial electric field variability, plotted in geomagnetic coordinates above  $60^\circ$  latitude and organized by IMF clock angle, hemisphere, and dipole tilt. In each map, the overall average variability magnitude is indicated at the bottom left. The IMF clock angle category is indicated at the top of each column.  $B_{y+/-}$  indicates IMF  $B_{y+}$  and  $B_{y-}$  in the Northern and Southern Hemispheres, respectively.

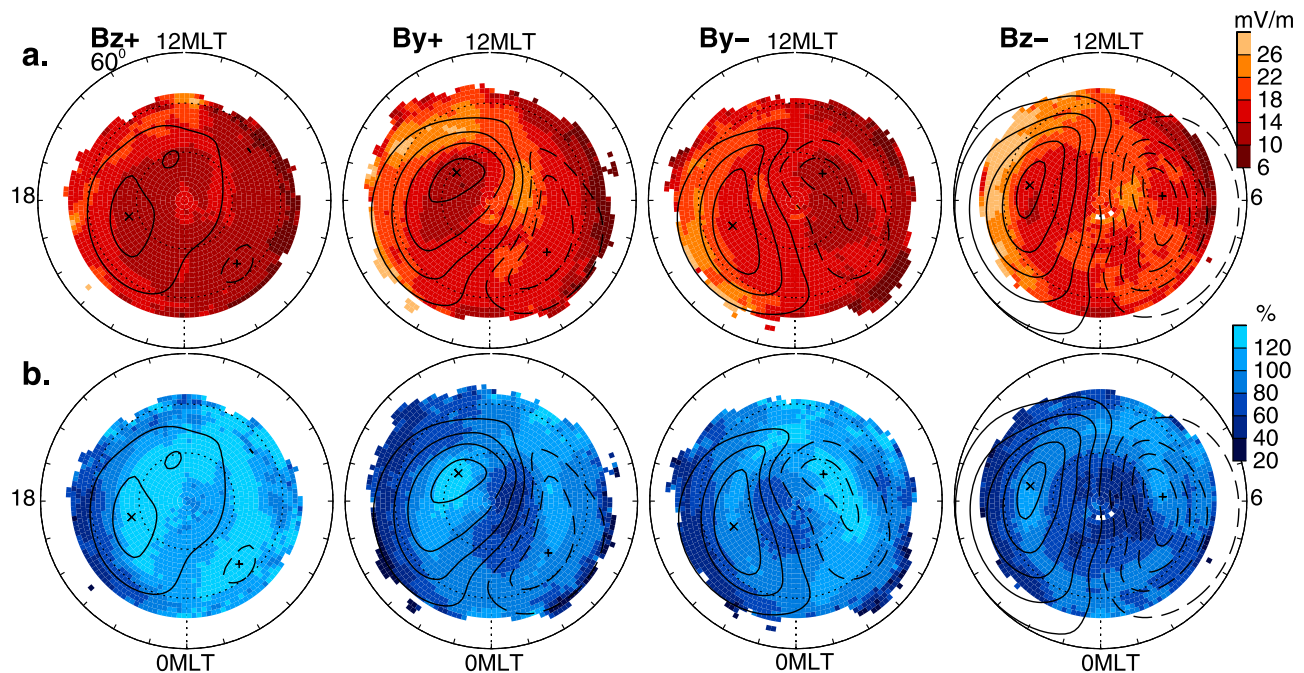


**Figure 4.** Maps of (a) the RMS average of background electric fields and (b) the RMS average of electric field fluctuations as a percentage of the background field, according to color scales at right. Electrostatic potential contours are overplotted at 6 kV increments based on the empirical large-scale convection model of *Cousins and Shepherd* [2010], keyed to the average solar wind conditions of each map. Maps are for the Northern Hemisphere under negative tilt conditions, with IMF condition indicated at the top.

than the observed variability and they do not show a consistent tilt dependence, such that measurement error effects are not expected to contribute to the observed tilt dependence of variability.

[34] In general, as seen in Figure 3, maps of electric field variability for the Northern Hemisphere are very similar to those for the Southern Hemisphere (after accounting for the antisymmetry with respect to IMF  $B_y$ ). Both hemispheres show the same general IMF clock angle and tilt dependencies and the average magnitudes of variability are similar in the two hemispheres. The average magnitudes of variability, however, tend to be slightly larger (by  $\sim 5\%$  on average) in the Southern than Northern Hemisphere for comparable conditions. The differences between hemispheres will be discussed more in section 4.

[35] The average small-scale electric field variability magnitudes shown in Figure 3 are on the same order of magnitude as, and in some cases larger than, the observed background electric field. Figure 4a shows example maps of the RMS average of the background electric fields, with the corresponding maps of the relative variability magnitude shown in Figure 4b. As a visual aid, electrostatic potential contours are overplotted at 6 kV increments in both Figures 4a and 4b based on the empirical large-scale convection model of *Cousins and Shepherd* [2010], keyed to the average solar wind conditions of each map. Under northward IMF conditions, when the background convection is weak, the RMS variability magnitudes are  $\sim 110\%$  relative to the RMS background fields with relative magnitudes reaching above 120% across the high polar cap. The smallest relative magnitudes of variability occur under southward IMF conditions, when the RMS variability magnitudes are

$\sim 75\%$  of the RMS background fields with relative magnitudes below 60% in the region of strong antisunward flow across the polar cap. For IMF  $B_y$  dominated conditions, the relative variability magnitudes are  $\sim 90\%$ , on average, with largest relative variability magnitudes occurring in regions of convection reversals, where the average background fields are small. Although the maps shown in Figure 4 are for the Northern Hemisphere under negative tilt conditions, similar results are observed for the Southern Hemisphere and for other dipole tilt conditions (with slightly ( $\sim 10\%$ ) smaller relative variability magnitudes occurring under positive tilt conditions). It is expected, therefore, that small-scale variability is a significant component of the total ionospheric electric field under all IMF and dipole tilt conditions.

[36] To better illustrate the tilt dependence of the maps of variability, the MLT and geomagnetic latitude distributions of variability across the range of tilt angles are shown in Figure 5 for the Northern and Southern Hemispheres. For Figures 5a and 5b, spatial variability data are sorted and averaged into 1 h MLT bins within  $10^\circ$  tilt bins, a finer tilt resolution than that used for the maps shown in Figure 3. For Figures 5c and 5d,  $2^\circ$  geomagnetic latitude bins are used within the same tilt bins. For these averages, only data from  $65^\circ$  to  $85^\circ$  latitude are included because this region contains data across the entire MLT and latitude ranges for all the finer-resolution tilt bins. Note that prior to sorting by MLT or latitude the original spatial variability data are averaged onto a  $\sim 110 \times 110$  km equal area grid such that all regions are weighted equally when averaged together.

[37] As shown in Figures 5a and 5b, variability values on the dayside (6–18 MLT) decrease the most from “winter” to “summer” while values on the nightside (0–6 MLT and

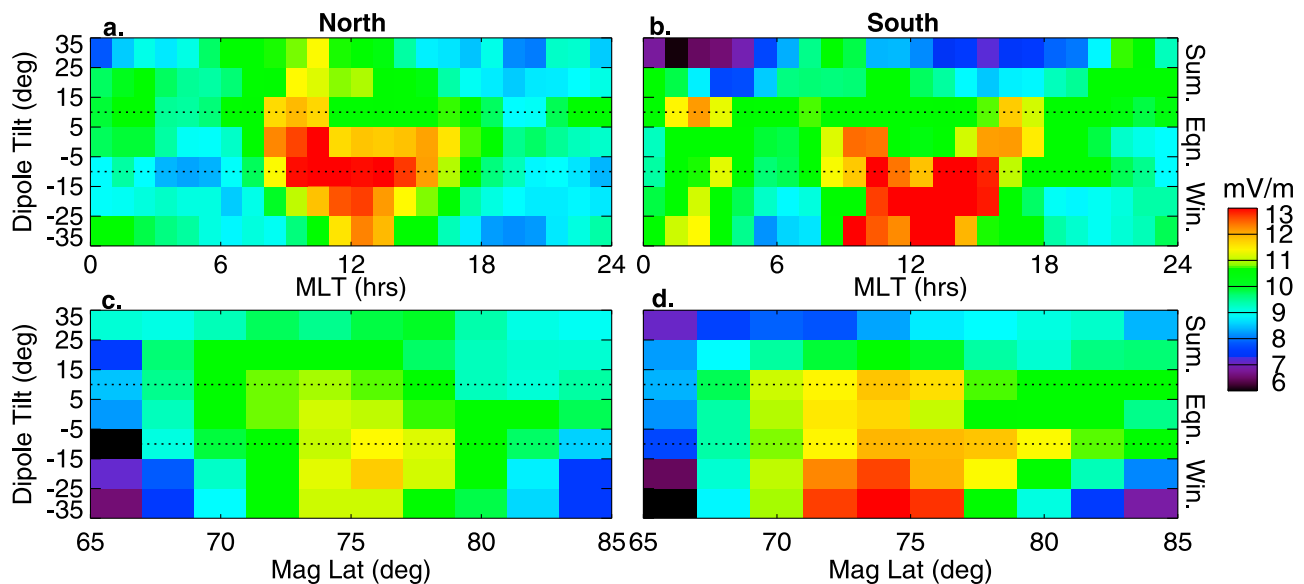


**Figure 5.** The tilt dependence of (a, b) the MLT distribution and (c, d) the latitude distribution of variability in the Northern and Southern Hemispheres. The color indicates the average variability magnitude according to the scale at the right. Dotted lines delineate the seasonal categories used in creating variability maps.

18–24 MLT) do not change significantly with increasing tilt. Considering the latitude dependence shown in Figures 5c and 5d, variability magnitudes in the auroral zone ( $70^{\circ}$ – $80^{\circ}$ ) decrease from “winter” to “summer” while values near the polar cap and near the lower latitude limit can be in fact larger for “summer” than for “winter”. In addition, the location of peak variability moves to higher latitudes for tilts near  $-15^{\circ}$  and tends to move equatorward as tilt increases. As a result of these tilt dependencies, the distribution of variability is much more uniform in latitude and MLT for “summer” than it is for “winter”. Comparing the variability maps for positive and negative tilt in Figure 3 also shows this relative uniformity in the spatial distribution of variability for positive tilt.

[38] Although the tilt dependencies shown in Figure 5 are generally similar between hemispheres, some differences are observed. For example, variability in the Southern Hemisphere (Figures 5b and 5d) is, on average, larger for large negative tilt and is smaller for large positive tilt than variability in the Northern Hemisphere (Figures 5a and 5c). This asymmetry is consistent with the stronger tilt dependence of electric field variability in the Southern than Northern Hemisphere observed by *Cousins and Shepherd* [2012] and will be discussed more in section 4.

#### 4. Discussion

[39] The possible origins of the spatial distributions of variability and of the IMF clock angle and dipole tilt dependencies described in section 3 are considered through comparison with other ionospheric parameters. In particular, possible relationships with large- and small-scale field-aligned currents and with velocity vorticity are considered. The results are also compared with those of other small-scale electric field variability studies. It should be noted, however, that the other variability studies to which the current results are compared are primarily based on satellite data, which

have an inherent space-time ambiguity. In the satellite-based studies, an assumption of convecting static structures is typically used to convert observed temporal variations to spatial variability. As a result, the variability maps derived in this study using ground-based data are not exactly equivalent to the variability maps derived in other studies based on satellite data. Furthermore, the observation that spatial and temporal variability have similar behaviors cannot be compared with results from previous satellite-based studies.

[40] As discussed by *Cousins and Shepherd* [2012], the strongest observed correlation of small-scale electric field variability is with gradients or shears in the background plasma drift. As a result, the spatial distribution of variability magnitudes is strongly correlated with the spatial distribution of velocity gradients or shears. (Note that the LOS measurements used in this study cannot distinguish between gradients and shears in velocity.) It is expected that the observed velocity gradients or shears are correlated to some extent with velocity vorticity, which can be correlated with field-aligned currents. *Chisham et al.* [2009] investigated velocity vorticity in SuperDARN data and found that the average spatial distribution of this vorticity appears very similar to that of average, large-scale field-aligned currents.

[41] The spatial distributions of small-scale electric field variability described in section 3 are qualitatively similar to average distributions of both velocity vorticity, as observed by *Chisham et al.* [2009] with SuperDARN data, and the large-scale region 1 field-aligned current (FAC) densities, as measured by low-altitude satellites. On average, large-scale region 1 FAC densities and velocity vorticity magnitudes tend to be enhanced in a band between  $\sim 70^{\circ}$  and  $80^{\circ}$  geomagnetic latitude, with downward current on the dawnside and upward current on the duskside in MLT [e.g., *Chisham et al.*, 2009; *Weimer*, 2001, 2005; *Korth et al.*, 2010]. For negative and neutral tilt, this region corresponds to the observed region of enhanced variability. For positive tilt,

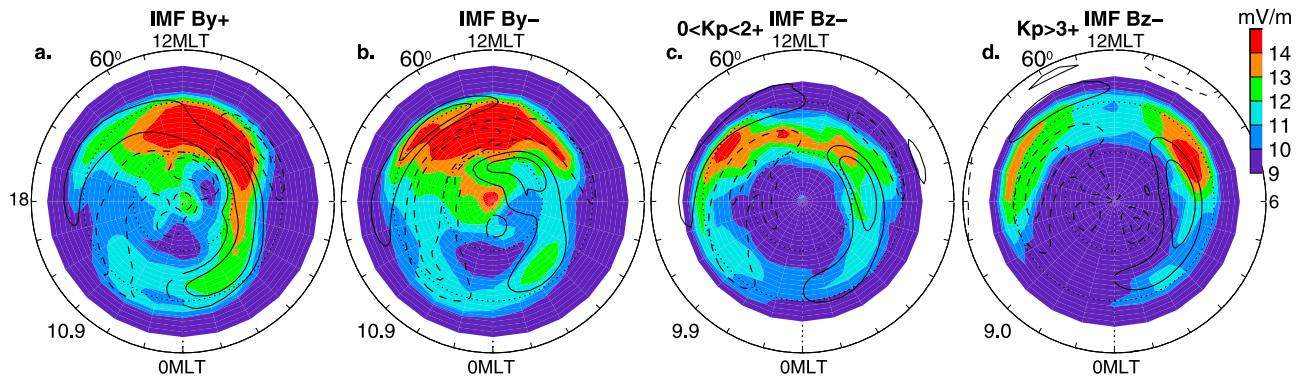


**Figure 6.** Fitted average magnitudes of small-scale spatial electric field variability for neutral tilt in the Northern Hemisphere, plotted in geomagnetic coordinates, with overlaid contours of a normalized FAC proxy. Solid lines indicate downward FAC, and dashed lines indicate upward FAC. In each map, the IMF clock angle category is indicated at the top, and the overall average variability magnitude is indicated at the bottom left.

however, variability magnitudes are less organized and do not appear correlated with FAC or vorticity distributions.

[42] Figure 6 shows Northern Hemisphere neutral tilt fitted variability maps overlaid with contours of a FAC proxy. This FAC proxy is obtained by calculating the electric field divergence from the empirical large-scale convection model of *Cousins and Shepherd* [2010] (with the convection pattern keyed to the average solar wind conditions of the variability maps), and the contours are plotted with normalized units. (Note that the maps shown in Figures 6a and 6b are the same as those shown in Figure 3 with different color scales, while the maps in Figures 6c and 6d have been subdivided by  $K_p$ , a global geomagnetic activity index.) Although an exact, one-to-one correlation between the FAC density proxy and variability magnitude is not observed, the region of enhanced variability is collocated with the region of enhanced FAC density. Furthermore, the IMF clock angle dependence and the  $K_p$  dependence of the variability maps appear similar to those of the large-scale FACs, as described here.

[43] The rotation in MLT of peak variability between IMF  $B_{y-}$  (Figure 6a) and  $B_{y+}$  (Figure 6b) coincides with the rotation of the cusp location [*Newell et al.*, 1989] and the rotation of the vorticity and FAC pattern [*Chisham et al.*, 2009; *Korth et al.*, 2010]. For northward IMF, both enhanced electric field variability and enhanced FAC densities can be observed across the polar cap, poleward of  $80^\circ$  (Figure 3, first column), while for southward IMF, enhanced variability and enhanced FAC densities are confined primarily to the auroral zone (Figure 6c). Under dominant IMF  $B_y$  conditions (Figures 6a and 6b), the dayside variability peak is larger than that under southward IMF (Figure 6c), possibly due to the wrapping of the FAC pattern around the dayside resulting from the different reconnection geometry during dominant IMF  $B_y$  conditions [e.g., *Potemra*, 1985]. Furthermore, if the electric field variability is sorted by geomagnetic activity level according to the  $K_p$  index (Figures 6c and 6d), while the average magnitudes of variability do not increase, the region of enhanced variability expands equatorward with increasing activity level. This expansion follows the expansion of the FAC pattern observed by *Korth et al.* [2010] for increasing solar wind

driving (as indicated by the solar wind electric field). A similar correlation between patterns of variability and FACs under varying IMF clock angles was also noted by *Golovchanskaya et al.* [2006], who calculated both small-scale electric field variability and large-scale FAC densities from DE-2 data.

[44] It is interesting to note, however, that the nightside distributions of small-scale electric field variability are not symmetric about the noon-midnight meridian. In general, as noted by *Cousins and Shepherd* [2012], nightside variability is larger on the dawnside than on the duskside. A similar dawn-dusk asymmetry was noted by *Matsuo and Richmond* [2008], who investigated small-scale (3–500 km) electric field variability in DE-2 data. This asymmetry could indicate that, on the nightside, downward FACs are preferential for enhancing small-scale electric field variability. The occurrence of enhanced small-scale electric field fluctuations in downward FAC regions has previously been observed in FAST [*Ergun et al.*, 1998] and Freja [*Marklund et al.*, 1997] satellite data and has been simulated numerically [*Streltsov and Lotko*, 2003; *Streltsov and Marklund*, 2006]. The electric field structures in these studies, however, are estimated to have a spatial scale on the order of 1 km, a much smaller scale than that used in this study, and their amplitudes are between 100 mV/m and 1 V/m, much larger than the magnitudes seen in this study. Furthermore, *Marklund et al.* [1997] observed that the amplitude of the electric field structures decreases with increasing scale size, while the opposite dependence was observed by *Cousins and Shepherd* [2012] for the electric field fluctuations considered in this study. These differences suggest that the electric field fluctuations described here are a different phenomenon than previously observed intense, very small scale electric field structures in downward FACs [*Ergun et al.*, 1998; *Marklund et al.*, 1997].

[45] The maps of small-scale electric field variability magnitude shown in Figure 3 are also qualitatively very similar to maps of mesoscale FAC density given by *Hasunuma et al.* [2008], who calculated FACs on scales from  $\sim 10$  to 100 km from Akebono satellite data mapped to ionospheric altitudes. The mesoscale FACs peak on the dayside and dawnside in auroral latitudes, like electric field

variability magnitudes seen here, and they have a similar dependence on IMF clock angle to that of electric field variability. *Hasunuma et al.* [2008] compared maps of mesoscale FACs to those of large-scale FACs and found a correlation between downward large-scale currents and enhanced mesoscale current densities. These results suggest that small-scale electric field fluctuations are correlated with mesoscale FACs, both of which appear enhanced in downward large-scale FACs.

[46] Although the spatial distribution of small-scale electric field variability appears correlated to the distributions of both velocity vorticity and large- and small-scale FAC densities, the seasonal dependence of electric field variability is observed to be opposite that of vorticity and FAC densities, which tend to be larger in the summer than in the winter [e.g., *Chisham et al.*, 2009; *Weimer*, 2001; *Hasunuma et al.*, 2008; *Juusola et al.*, 2009]. Furthermore, while the morphologies of vorticity and of large- and small-scale FACs do not change significantly between winter and summer, the morphology of small-scale electric field variability magnitudes does change, becoming less organized in the “summer” as compared to in the “winter”. A similar change in the morphology of electric field variability magnitudes was also observed by *Matsuo and Richmond* [2008] in DE-2 data (compare Figure 2 with Figure 4 in that paper).

[47] Several factors could account for the observed tilt dependence of electric field variability. On the nightside and at small scales, the magnetosphere is thought to act like a current source [*Lysak*, 1985; *Vickrey et al.*, 1986; *Liou et al.*, 2001]. In this regime, as conductivity increases (during summer-like, positive tilt conditions) the electric field required to sustain constant current decreases. This picture is consistent with the observations of decreased small-scale electric fields for positive tilt. The observations of increased (not constant) small-scale FAC densities in summer [*Hasunuma et al.*, 2008], however, are not consistent with this idea of a constant current source. Furthermore, this explanation does not account for the change in morphology of variability maps, especially because the dayside variability is observed to change more with tilt than the nightside variability while the nightside is thought to act more like a current source than the dayside.

[48] Another factor that could cause a tilt dependence in electric field variability is the existence of scale-size- and conductivity-dependent field-aligned potential drops, as discussed by *Weimer et al.* [1985] and *Vickrey et al.* [1986]. These field-aligned potential drops could cause small-scale electric field variability to be more attenuated in summer-like, positive tilt conditions. This theory is consistent with observations that electric field variability has greater tilt dependence at smaller scales than at larger scales. In this study, variability on scales from 45 to 90 km is 16% (32%) larger for negative than for positive tilt conditions in the north (south) while variability on scales from 360 to 450 km is only 4% (17%) larger for negative tilt conditions. *Matsuo and Richmond* [2008] also observed that variability (including scales from 3 to 500 km) increases significantly from “summer” to “winter” while variability on larger scales does not, consistent with the results of this study. The existence of such scale-size-dependent field-aligned potential drops is also consistent with the observed small-scale variability being smaller for positive than for negative tilts,

even while the average magnitudes of larger-scale background velocity gradients or shears (with scale sizes on the order of 1000 km) do not decrease. Furthermore, the relative magnitudes of small-scale variability as compared to the large-scale background electric field are also smaller for positive than for negative tilts. It is not clear, however, how field-aligned potential drops could account for the observed change in the morphology of variability maps, which become more uniform and less organized for positive as compared to negative tilt conditions.

[49] Finally, the tilt dependence that is observed in the electric field variability could be due to a “seasonal” change in the processes that generate variability. Such a change is suggested by observations of differences in the spatial distributions of variability under positive and negative tilt (see Figures 3 and 5). Note that the spatial distribution of observed velocity gradients or shears (possible sources of variability) also changes with tilt, being more organized for negative than for positive tilts. A change in the processes that generate variability could result from the very low conductivities in negative tilt, winter-like conditions (particularly in downward current regions) that could allow for instabilities to be triggered more easily [e.g., *Streltsov and Lotko*, 2003; *Streltsov and Marklund*, 2006]. It is also expected that the ionospheric conductivity is more structured in winter-like conditions when the solar extreme ultraviolet (EUV) input is less dominant, and this conductivity structure could contribute to the observed electric field variability.

[50] Although the exact mechanisms that cause a tilt dependence in the magnitudes and spatial distribution of small-scale electric field variability are not fully understood, the observations discussed here suggest that scale-size and conductivity-dependent field-aligned potential drops, changes in the processes that generate variability, or more likely some combination of the two effects plays a role. The observed tilt dependence, however, which is more significant on the dayside than on the nightside, does not appear to be the result of a constant current source in the magnetosphere.

[51] The tilt dependence in observed electric field variability is generally symmetric between hemispheres, such that northern “winter” is roughly equivalent to southern “winter” and northern “summer” to southern “summer”. After accounting for the opposite signs of dipole tilt in the two hemispheres, however, some interhemispheric asymmetries are still observed. As described in section 3, the primary differences are that a larger tilt dependence and slightly larger average variability magnitudes are observed in the Southern Hemisphere than in the Northern Hemisphere. These results are somewhat consistent with those of *Golovchanskaya* [2007], who, using DE-2 electric field data on scales from 3.8 to 100 km, observed slightly larger average variability in the Southern Hemisphere than in the Northern Hemisphere. The seasonal dependence of variability, however, was observed to be approximately the same in the two hemispheres in that study. The differences between variability in the two hemispheres observed in this study could be the result of interhemispheric asymmetries in the geomagnetic field. As discussed by *Cousins and Shepherd* [2012], the offset between the magnetic pole and geographic pole is larger in the Southern than Northern Hemisphere, possibly contributing to the larger tilt dependence in this hemisphere. Additionally, in the region considered in this study, the Earth’s magnetic field is on average ~5% larger

in the Southern Hemisphere than it is in the Northern Hemisphere, possibly contributing to the difference in the observed average variability magnitudes.

## 5. Summary

[52] In this study, we investigate the spatial distributions of ionospheric small-scale electric field variability in the high-latitude regions of the Northern and Southern hemispheres using SuperDARN line-of-sight velocity data from 1999 to 2004. Maps of average variability magnitudes are derived independently in the two hemispheres for 12 dipole tilt angle and IMF clock angle categories. In general, the observed variability magnitudes are largest on the dayside and in the auroral zone and are larger, on average, for negative tilt (winter-like) conditions than for positive tilt (summer-like) conditions. These average variability magnitudes are found to be on the same order of magnitude as the large-scale background electric fields, with relative RMS magnitudes ranging from  $\leq 60\%$  (in the strong antisunward drifts across the polar cap under southward IMF, positive tilt conditions) to  $>120\%$  (in the polar cap under northward IMF, negative tilt conditions).

[53] Under negative tilt and neutral tilt conditions, the spatial distributions of small-scale electric field variability magnitudes appear correlated to those of region 1 FACs, with the variability maps showing a similar dependence on IMF clock angle and on geomagnetic activity level as that of FAC distributions. On the nightside, auroral zone variability tends to be larger on the dawnside than duskside, suggesting that downward FACs may be preferable for enhanced electric field variability. During positive tilt (summer-like) conditions, variability values (on the dayside in particular) are smaller than during negative tilt, and the spatial distribution tends to be less organized and more uniform across the high-latitude region independent of IMF clock angle. These dipole tilt dependencies suggest that scale-size- and conductivity-dependent field-aligned potential drops, as well as seasonal changes in the processes that generate variability, may impact the variability observed in the  $F$  region ionosphere.

[54] For all IMF and tilt categories, Southern Hemisphere maps appear very similar to Northern Hemisphere maps, although a larger tilt dependence and slightly larger average variability magnitudes are observed in the Southern than Northern Hemisphere, possibly resulting from interhemispheric asymmetries in the geomagnetic field.

[55] **Acknowledgments.** Operation of the SuperDARN radars is supported by the national funding agencies of the U.S., Canada, UK, France, Japan, Italy, South Africa, and Australia. We gratefully acknowledge the CDAWeb for providing the high-resolution OMNI data used in this study. This work was supported by NSF grants ATM-0836485 and ATM-0838356 and NASA grant NNX-10AL97H.

[56] Robert Lysak thanks the reviewers for their assistance in evaluating this paper.

## References

- Abel, G. A., M. P. Freeman, G. Chisham, and N. W. Watkins (2007), Investigating turbulent structure of ionospheric plasma velocity using the Halley SuperDARN radar, *Nonlinear Processes Geophys.*, *14*(6), 799–809.
- Abel, G. A., M. P. Freeman, and G. Chisham (2009), IMF clock angle control of multifractality in ionospheric velocity fluctuations, *Geophys. Res. Lett.*, *36*, L19102, doi:10.1029/2009GL040336.
- Baker, K. B., and S. Wing (1989), A new coordinate system for conjugate studies at high latitudes, *J. Geophys. Res.*, *94*, 9139.
- Chisham, G., M. P. Freeman, G. A. Abel, W. A. Bristow, A. Marchaudon, J. M. Ruohoniemi, and G. J. Sofko (2009), Spatial distribution of average vorticity in the high-latitude ionosphere and its variation with interplanetary magnetic field direction and season, *J. Geophys. Res.*, *114*, A09301, doi:10.1029/2009JA014263.
- Codrescu, M. V., T. J. Fuller-Rowell, and J. C. Foster (1995), On the importance of E-field variability for Joule heating in the high-latitude thermosphere, *Geophys. Res. Lett.*, *22*, 2393.
- Codrescu, M. V., T. J. Fuller-Rowell, J. C. Foster, J. M. Holt, and S. J. Cariglia (2000), Electric field variability associated with the Millstone Hill electric field model, *J. Geophys. Res.*, *105*, 5265.
- Codrescu, M. V., T. J. Fuller-Rowell, V. Munteanu, C. F. Minter, and G. H. Millward (2008), Validation of the Coupled Thermosphere Ionosphere Plasmasphere Electrodynamics model: CTIPE-mass spectrometer incoherent scatter temperature comparison, *Space Weather*, *6*, S09005, doi:10.1029/2007SW000364.
- Cosgrove, R., M. McCreedy, R. Tsunoda, and A. Stromme (2011), The bias on the Joule heating estimate: Small-scale variability versus resolved-scale model uncertainty and the correlation of electric field and conductance, *J. Geophys. Res.*, *116*, A09320, doi:10.1029/2011JA016665.
- Cousins, E. D. P., and S. G. Shepherd (2010), A dynamical model of high-latitude convection derived from SuperDARN plasma drift measurements, *J. Geophys. Res.*, *115*, A12329, doi:10.1029/2010JA016017.
- Cousins, E. D. P., and S. G. Shepherd (2012), Statistical characteristics of small-scale spatial and temporal electric field variability in the high-latitude ionospheres, *J. Geophys. Res.*, *117*, A03317, doi:10.1029/2011JA017383.
- Deng, Y., and A. J. Ridley (2007), Possible reasons for underestimating Joule heating in global models: E field variability, spatial resolution, and vertical velocity, *J. Geophys. Res.*, *112*, A09308, doi:10.1029/2006JA012006.
- Deng, Y., A. Maute, A. D. Richmond, and R. G. Roble (2009), Impact of electric field variability on Joule heating and thermospheric temperature and density, *Geophys. Res. Lett.*, *36*, L08105, doi:10.1029/2008GL036916.
- Earle, G. D., and M. C. Kelley (1993), Spectral evidence for stirring scales and two-dimensional turbulence in the auroral ionosphere, *J. Geophys. Res.*, *98*, 11,543.
- Efron, B., and R. J. Tibshirani (1993), *An Introduction to the Bootstrap*, CRC Press, Boca Raton, Fla.
- Ergun, R. E., et al. (1998), FAST satellite observations of large-amplitude solitary structures, *Geophys. Res. Lett.*, *25*, 2041.
- Fedrizzi, M., T. J. Fuller-Rowell, and M. V. Codrescu (2012), Global Joule heating index derived from thermospheric density physics-based modeling and observations, *Space Weather*, *10*, S03001, doi:10.1029/2011SW000724.
- Fesen, C. G., B. A. Emery, M. J. Buonsanto, Q. H. Zhou, and M. P. Sulzer (1999), Simulations of the F region during the January 1993 10-day campaign, *J. Geophys. Res.*, *102*, 7249.
- Fuller-Rowell, T. J., and D. Rees (1980), A 3-dimensional time-dependent global-model of the thermosphere, *J. Atmos. Sci.*, *37*, 2545.
- Golovchanskaya, I. V. (2007), On the seasonal variation of electric and magnetic turbulence at high latitudes, *Geophys. Res. Lett.*, *34*, L13103, doi:10.1029/2007GL030125.
- Golovchanskaya, I. V., Y. P. Maltsev, and A. A. Ostapenko (2002), High-latitude irregularities of the magnetospheric electric field and their relation to solar wind and geomagnetic conditions, *J. Geophys. Res.*, *107*(A1), 1001, doi:10.1029/2001JA900097.
- Golovchanskaya, I. V., A. A. Ostapenko, and B. V. Kozelov (2006), Relationship between the high-latitude electric and magnetic turbulence and the Birkeland field-aligned currents, *J. Geophys. Res.*, *111*, A12301, doi:10.1029/2006JA011835.
- Hasunuma, T., T. Nagatsuma, R. Kataoka, Y. Takahashi, H. Fukunishi, A. Matsuoka, and A. Kumamoto (2008), Statistical study of polar distribution of mesoscale field-aligned currents, *J. Geophys. Res.*, *113*, A12214, doi:10.1029/2008JA013358.
- Heppner, J. P., M. C. Liebrecht, N. C. Maynard, and R. F. Pfaff (1993), High-latitude distributions of plasma waves and spatial irregularities from DE2 alternating current electric field observations, *J. Geophys. Res.*, *98*, 1629.
- Ishii, M., M. Sugiura, T. Iyemori, and J. Slavin (1992), Correlation between magnetic and electric-field perturbations in the field-aligned current regions deduced from DE 2 observations, *J. Geophys. Res.*, *97*(A9), 13,877.
- Johnson, E., and R. Heelis (2005), Characteristics of ion velocity structure at high latitudes during steady southward interplanetary magnetic field conditions, *J. Geophys. Res.*, *110*, A12301, doi:10.1029/2005JA011130.
- Juusola, L., K. Kauristie, O. Amm, and P. Ritter (2009), Statistical dependence of auroral ionospheric currents on solar wind and geomagnetic

- parameters from 5 years of CHAMP satellite data, *Ann. Geophys.*, *27*, 1005.
- King, J. H., and N. E. Papitashvili (2005), Solar wind spatial scales in and comparisons of hourly Wind and ACE plasma and magnetic field data, *J. Geophys. Res.*, *110*, A02104, doi:10.1029/2004JA010649.
- Knudsen, D., M. Kelley, G. Earle, J. Vickrey, and M. Boehm (1990), Distinguishing Alfvén waves from quasi-static field structures associated with the discrete aurora-sounding rocket and HILAT satellite measurements, *Geophys. Res. Lett.*, *17*(7), 921.
- Korth, H., B. J. Anderson, and C. L. Waters (2010), Statistical analysis of the dependence of large-scale Birkeland currents on solar wind parameters, *Ann. Geophys.*, *28*, 515.
- Liou, K., P. T. Newell, and C.-I. Meng (2001), Seasonal effects on auroral particle acceleration and precipitation, *J. Geophys. Res.*, *106*, 5531.
- Lysak, R. L. (1985), Auroral electrodynamics with current and voltage generators, *J. Geophys. Res.*, *90*, 4178.
- Marklund, G., T. Karlsson, and J. Clemmons (1997), On low-altitude particle acceleration and intense electric fields and their relationship to black aurora, *J. Geophys. Res.*, *102*, 17,509.
- Matsuo, T., and A. D. Richmond (2008), Effects of high-latitude ionospheric electric field variability on global thermospheric Joule heating and mechanical energy transfer rate, *J. Geophys. Res.*, *113*, A07309, doi:10.1029/2007JA012993.
- Matsuo, T., A. D. Richmond, and D. W. Nychka (2002), Modes of high-latitude electric field variability derived from DE-2 measurements: Empirical orthogonal function (EOF) analysis, *Geophys. Res. Lett.*, *29*(7), 1107, doi:10.1029/2001GL014077.
- Matsuo, T., A. D. Richmond, and K. Hensel (2003), High-latitude ionospheric electric field variability and electric potential derived from DE-2 plasma drift measurements: Dependence on IMF and dipole tilt, *J. Geophys. Res.*, *108*(A1), 1005, doi:10.1029/2002JA009429.
- Newell, P. T., C.-I. Meng, D. G. Sibeck, and R. Lepping (1989), Some low-altitude cusp dependencies on the interplanetary magnetic field, *J. Geophys. Res.*, *94*, 8921.
- Papitashvili, V. O., F. J. Rich, M. A. Heinemann, and M. R. Hairston (1999), Parameterization of the Defense Meteorological Satellite Program ionospheric electrostatic potentials by the interplanetary magnetic field strength and direction, *J. Geophys. Res.*, *104*, 177.
- Parkinson, M. L. (2008), Complexity in the scaling of velocity fluctuations in the high-latitude F-region ionosphere, *Ann. Geophys.*, *26*(9), 2657–2672.
- Pettigrew, E. D., S. G. Shepherd, and J. M. Ruohoniemi (2010), Climatological patterns of high-latitude convection in the Northern and Southern Hemispheres: Dipole tilt dependencies and interhemispheric comparisons, *J. Geophys. Res.*, *115*, A07305, doi:10.1029/2009JA014956.
- Potemra, T. A. (1985), Field-aligned (Birkeland) currents, *Space Sci. Rev.*, *42*, 295.
- Ridley, A. J., Y. Deng, and G. Tóth (2006), The global ionosphere-thermosphere model, *J. Atmos. Sol. Terr. Phys.*, *68*, 839.
- Roble, R. G., E. C. Ridley, A. D. Richmond, and R. E. Dickinson (1988), A coupled thermosphere/ionosphere general circulation model, *Geophys. Res. Lett.*, *15*, 1325.
- Ruohoniemi, J. M., and R. A. Greenwald (1997), Rates of scattering occurrence in routine HF radar observations during solar cycle maximum, *Radio Sci.*, *32*, 1051.
- Ruohoniemi, J. M., and R. A. Greenwald (1998), The response of high-latitude convection to a sudden southward IMF turning, *Geophys. Res. Lett.*, *25*, 2913.
- Ruohoniemi, J. M., and R. A. Greenwald (2005), Dependencies of high-latitude plasma convection: Consideration of interplanetary magnetic field, seasonal, and universal time factors in statistical patterns, *J. Geophys. Res.*, *110*, A09204, doi:10.1029/2004JA010815.
- Shepherd, S. G., and J. M. Ruohoniemi (2000), Electrostatic potential patterns in the high latitude ionosphere constrained by SuperDARN measurements, *J. Geophys. Res.*, *105*, 23,005.
- Streltsov, A. V., and W. Lotko (2003), Small-scale electric fields in downward auroral current channels, *J. Geophys. Res.*, *108*(A7), 1289, doi:10.1029/2002JA009806.
- Streltsov, A. V., and G. T. Marklund (2006), Divergent electric fields in downward current channels, *J. Geophys. Res.*, *111*, A07204, doi:10.1029/2005JA011196.
- Vickrey, J. F., R. C. Livingston, N. B. Walker, T. A. Potemra, R. A. Heelis, M. C. Kelley, and F. J. Rich (1986), On the current voltage relationship of the magnetospheric generator at intermediate spatial scales, *Geophys. Res. Lett.*, *13*, 495.
- Weimer, D. R. (2001), Maps of ionospheric field-aligned currents as a function of the interplanetary magnetic field derived from Dynamics Explorer 2 data, *J. Geophys. Res.*, *106*, 12,889.
- Weimer, D. R. (2005), Improved ionospheric electrodynamic models and application to calculating Joule heating rates, *J. Geophys. Res.*, *110*, A05306, doi:10.1029/2004JA010884.
- Weimer, D., C. Goertz, D. Gurnett, N. Maynard, and J. Burch (1985), Auroral-zone electric-fields from DE-1 and DE-2 at magnetic conjunctions, *J. Geophys. Res.*, *90*(A8), 7479.
- Zhang, S.-R., J. M. Holt, and M. McCready (2007), High latitude convection based on long-term incoherent scatter radar observations in North America, *J. Atmos. Sol. Terr. Phys.*, *69*, 1273.